machines

MDPI

Article

Two-Dimensional Analytical Models for Cogging Torque Prediction in Interior Permanent Magnet Machine

Linwei Wang, Shuai Lu * and Yangming Chen

School of Electrical Engineering, Chongqing University, Chongqing 400044, China
* Correspondence: shuai.lu@cqu.edu.cn; Tel.: +86-186-2352-2930

Abstract: Analytical prediction of cogging torque needs accurate flux density and relative permeance closed-form expressions. The accurate two-dimensional (2D) air gap flux density distribution function and the 2D permeance function are currently almost always applied to surface-mounted permanent magnet (SPM) machines, instead of interior permanent magnet (IPM) machines, due to complications from IPMs severe magnetic saturation and leakage flux. To address these issues, this paper proposes a set of new methods to derive the accurate closed-form 2D expressions of IPMs for both flux density and relative permeance. As for the flux density 2D model, a virtual equivalence model for IPM is introduced, so that Laplace's equation and quasi-Poisson equation can be directly applied to IPM. As for permeance, the same virtual equivalence model also enables 2D models derivation for IPM. Subsequently, the resulting cogging torque analytical expression is obtained with the accurate relative permeance and air gap flux density models. The results from the proposed 2D analytical models showed similar accuracy to the finite element analysis (FEA). In addition, as demonstrated, the proposed 2D analytical models is a highly efficient tool set in the design process of cogging torque optimization, facilitating fast evaluation of different design factors.

Keywords: cogging torque; two-dimensional permeance function; virtual equivalence model; interior permanent magnet machine

Citation: Wang, L.; Lu, S.; Chen, Y. Two-Dimensional Analytical Models for Cogging Torque Prediction in Interior Permanent Magnet Machine. *Machines* **2023**, *11*, 233. https://doi.org/10.3390/machines11020233

Academic Editor: Davide Astolfi

Received: 9 January 2023
Revised: 2 February 2023
Accepted: 2 February 2023
Published: 4 February 2023

1. Introduction

Permanent magnet (PM) machines featuring high efficiency, power, and torque density, have been widely used in industrial applications [1–3]. Compared to surface-mounted PM (SPM) machines, interior PM (IPM) machines have higher reluctance torque and wider constant power range, so they are well-suited for electric vehicles (EVs) traction drives. However, the undesired cogging torque due to the slotting effect causes vibration and noise [4]. Therefore, several cogging torque reduction design methods have been proposed [5–11]. Typical methods can be summarized as follows: pole-slot combination [7], pole-arc optimization [12], slot-opening optimization [13], slots or magnets skewing [14–16], magnet or slot-opening shifting [17–19], auxiliary slots [20], teeth pairing [21], etc.

Intensive design iteration for cogging torque reduction calls for highly efficient analytical models to accurately predict cogging torque, while the time-consuming FEA methods are only preferred when performing the final verification of the analytical results. Analytical models of cogging torque need accurate flux density and relative permeance closed-form expressions.

As for SPM flux density, the lumped magnetic circuit (LMC) method is usually used to derive one-dimensional (1D) flux density expression [22–24]. Qu et al. [25] have deduced the analytical expressions for the one-dimensional (1D) flux density within the air gap and magnets in an SPM machine using the LMC method. However, 1D models return rectangular distribution of air gap flux density, instead of the trapezoidal form obtained through FEA analysis. Therefore, the two-dimensional (2D) models are needed to obtain the accurate flux density distribution. Zhu et al. [26] have derived the analytical expressions

of 2D magnet field distributions produced by the PMs and the stator windings in SPM machines. Rahideh et al. [27] have calculated analytically the open circuit 2D magnet field distribution in five annular regions for slotless brushless SPM machines. Kim et al. [28] have obtained the 2D flux density distribution in SPM brushless dc motors by considering the slotting effects and rotor eccentric effects.

As for SPM permeance, the effect of slotting is analyzed when deriving the relative air gap permeance function. In [28] and [29], the 1D relative permeance function was obtained, respectively. However, the results from 1D model are always smaller than FEA results, because of the interpolar leakage flux, and the fact that the interface between the PMs and the air gap is no longer an equipotential surface. Therefore, Wang et al. [30] have derived the 2D relative permeance function in SPM brushless dc motors. Zhu et al. [31] have also proposed the refined relative permeance 2D model for SPM machines. The analytical results of the 2D model were in good agreement with FEA results.

However, the accurate two-dimensional (2D) models for both air gap flux density distribution and the 2D permeance discussed above are currently all applied to SPM machines. As for IPM machines, few studies exist, and only 1D models have been studied, due to complications from IPMs severe magnetic saturation and leakage flux. Zhu et al. [22] have proposed an improved LMC model to predict rapidly the open circuit air gap flux density in IPM with multilayer and multisegmented PMs. However, the 1D model does not consider the slotting effect and the air gap flux density is assumed to be an ideal rectangular distribution, which will lead to a significant error during cogging torque calculation. Seo et al. [32] have obtained flux density by the LMC method and predicted cogging torque by the lateral force method (LFM). However, the cogging torque predicted by 1D relative permeance and the rectangular flux density models had a significant deviation from the FEA results.

In this paper, 2D analytical models for IPM slotless air gap flux density and relative permeance are proposed to obtain accurate IPM cogging torque expressions. The key is to first configure a virtual SPM model with the same air gap flux distribution as the IPM, so that the 2D models for both IPM slotless air gap flux density and relative permeance can be derived, despite all the complications from IPM severe magnetic saturation and leakage flux.

The contribution of the proposed method can be summarized by comparison with the existing methods of IPM cogging torque analytical prediction. Both the air gap flux density distribution and permeance functions in the existing methods are all based on 1D models, which introduce significant deviations from the FEA results. By comparison, the proposed method introduces the 2D air gap flux density distribution and the 2D permeance functions for IPM. Therefore, the resulting cogging torque analytical prediction matches the FEA results well.

In Section 2, the existing 1D models for both slotless air gap flux density and relative permeance are analyzed and their limitations are discussed. In Section 3, the virtual SPM and its configuration process are proposed to achieve the equivalent radial air gap flux distribution as the original IPM. Then, Laplace's and quasi-Poisson equations are applied to virtual SPM to obtain the 2D slotless air gap flux density. Meanwhile, the same virtual SPM model is also applied to obtain the 2D relative permeance function. Finally, the resultant cogging torque can be obtained based on the proposed 2D model. In Section 4, the cogging torque patterns predicted by the proposed IPM 2D models are compared with FEA results. Three machines with different pole-slot combinations are studied. Then, the cogging torque optimization process using the proposed 2D analytical models is demonstrated by adjusting the pole-arc coefficient and slot-opening coefficient, respectively. Section 5 concludes the paper.

2. Existing Analytical Model for IPM Machine

2.1. Basic Magnetic Circuit Model

There are many types of rotor structures in IPM machines. In this paper, the V-type structure was selected, and the relevant parameters are given in Table 1. Figure 1 shows the IPM machine topology and the open circuit flux lines distribution.

Table 1. Main parameters of the selected machines.

Symbol	Quantity	Value
p	Number of pole-pair	4
N_s	Number of slots	12/36/48
D_1	Outer diameter of stator	269.24 mm
D_{i1}	Inner diameter of stator	161.9 mm
D_2	Outer diameter of rotor	160.4 mm
D_{i2}	Inner diameter of rotor	110.64 mm
L_{ef}	Machine active length	83.82 mm
δ	Air gap length	0.75 mm
ω_m	Magnet width	16 mm
h_m	Magnet thickness	6.48 mm
α_p	Pole-arc coefficient	0.63
α_s	Slot-opening coefficient	0.18
B_r	Magnet remanence	1.191 T
μ_r	Magnet relative permeability	1.03

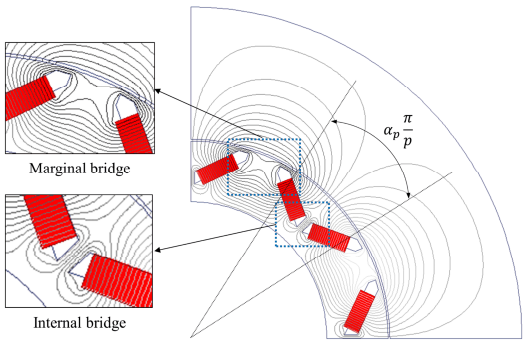

Figure 1. Open-circuit flux lines distribution of an IPM machine with slotless structure.

For IPM machines, the 1D LMC analytical method has been widely used. The LMC analysis is based on the following assumptions: the air gap flux density is only produced by PM (i.e., open circuit case) and the stator is slotless. As seen from the insets in Figure 1, there are many leakage fluxes across the marginal bridge and internal bridge. Based on the Ohm's law of magnetic circuit and the circuit symmetry, the simplified equivalent model is shown in Figure 2. Herein, ϕ_r is the magnetic flux source over a magnet pole, ϕ_{mib} and ϕ_{meb} are the leakage fluxes across the internal and marginal bridge, respectively. The corresponding reluctances are R_{mib} and R_{meb}.ϕ_{1ml} and ϕ_{2ml} are the magnet end leakage fluxes and the corresponding reluctances are R_{1ml} and R_{2ml}.ϕ_g and ϕ_{mo} are the air gap fluxes and leakage fluxes over a magnet pole. The corresponding reluctances are R_g and R_{mo}.

In consideration of the highly saturated bridges, the leakage flux through the bridges can be calculated as in [23,33,34]:

$$\phi_{mib} = \phi_{meb} = B_{sat} A_{bridge} \tag{1}$$

where A_{bridge} is the bridge's cross-sectional area and B_{sat} is the saturation level on the B-H curve of steel lamination. Analytical expressions of the lumped parameters in Figure 2 can be easily derived [22,35,36].

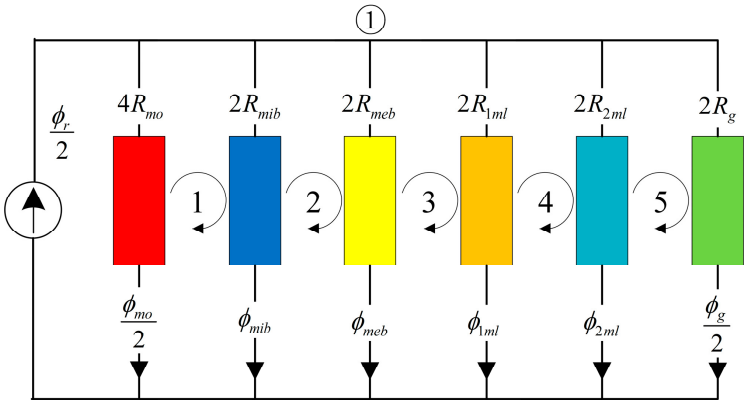

Figure 2. The simplified equivalent model based on LMC method.

2.2. One-Dimensional (1D) Model

Accurate slotted radial air gap flux density expression is needed for the subsequent cogging torque expression derivation using the net lateral force method and the superposition method. The slotted radial air gap flux density is calculated by the product of both the slotless radial air gap flux density and the relative permeance functions. Therefore, they are discussed as below.

2.2.1. Slotless Radial Air-Gap Flux Density

Based on the magnetic field periodicity, the 1D radial slotless air gap flux density can be expressed by a Fourier series expansion as:

$$B_{r\_1D}(\theta) = \sum_{n=1,3,5\ldots}^{\infty} 2B_n \cos(np\theta) \tag{2}$$

and

$$B_n = B_{r\_amp\_1D} \cdot \alpha_p \frac{\sin(n\pi\alpha_p)}{\frac{n\pi\alpha_p}{2}} \tag{3}$$

where p is the pole-pair number, α_p is the pole-arc coefficient, and $B_{r\_amp\_1D}$ is obtained by the LMC method.

Figure 3 shows the 1D model slotless radial air gap flux density results in comparison with FEA. Obviously, the rectangular air gap flux density using 1D model does not match the trapezoidal form in FEA result. This is because 1D model does not consider inter-polar leakage flux, which would require 2D models using Laplace's equation and quasi-Poisson equation.

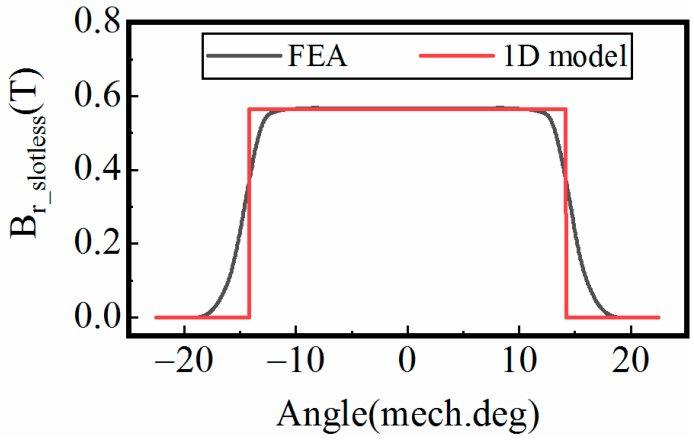

Figure 3. The 1D model slotless radial air gap flux density results comparison with FEA.

2.2.2. Relative Permeance Function

In the 1D model, the relative permeance function can be calculated as:

$$\widetilde{G}_{1D}(\theta) = \frac{G_{1D}(\theta)}{\mu_0/(\delta + h_m/\mu_r)} = \begin{cases} 1 & (\mathrm{n}-1)\theta_{tp} + \theta_{so}/2 \le \theta \le n\theta_{tp} - \theta_{so}/2 \\ \frac{\delta + h_m/\mu_r}{\delta(\theta) + h_m/\mu_r} & (\mathrm{n}-1)\theta_{tp} - \theta_{so}/2 \le \theta \le (\mathrm{n}-1)\theta_{tp} + \theta_{so}/2 \end{cases} \quad (4)$$

where $n = 1, 2, \ldots\ N_s$, θ_{tp} is the stator tooth pitch angle, θ_{so} is the slot opening angle, R_{i1} is the inner radius of stator, and $\delta(\theta) = \delta + \frac{\pi R_{i1}}{2}\left\{\frac{\theta_{so}}{2} - \left[|\theta| - (\mathrm{n}-1)\theta_{tp}\right]\right\}$.

Figure 4 shows the relative permeance comparison of 1D model and FEA result. Obviously, the permeance plot using 1D model does not match that of the FEA result. There are two reasons. First, due to the interpolar leakage flux, the PM working point is no longer constant. Second, the interface between the PMs and the air gap is no longer an equipotential surface. Therefore, the 2D models using the carter coefficient and the Schwarz–Christoffel Transformation are needed to address these complications.

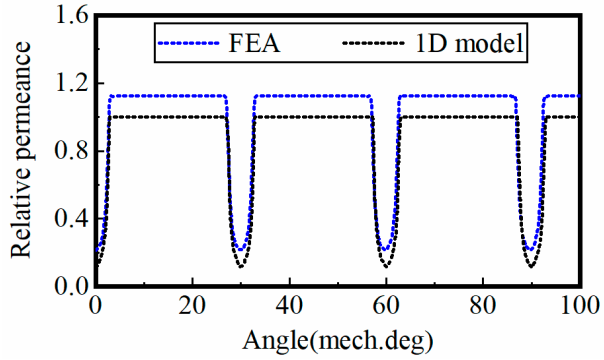

Figure 4. The 1D model relative permeance results comparison with FEA.

2.2.3. Summary

As discussed above, both the radial air gap flux density and the relative permeance of IPM need 2D models to be reasonably accurate for cogging torque prediction. However, due to significant leakage flux and magnetic saturation in IPM machines, it is very difficult to employ those 2D analytical methods to predict both the open circuit air gap flux density and the relative permeance. This is also the reason why there are no such 2D model for IPM in the existing literature.

3. Proposed Method of IPM Cogging Torque Analytical Prediction

In this paper, to obtain accurate IPM cogging torque expressions, 2D analytical models for IPM slotless radial air gap flux density and relative permeance are proposed. The key was to first configure a virtual SPM model with the same radial air gap flux distribution as the IPM, so that the 2D models for both IPM slotless radial air gap flux density and relative permeance could be derived, despite all the complications from IPM severe magnetic saturation and leakage flux.

3.1. Slotless Radial Air-Gap Flux Density Function Based on the 2D Model

Figure 5a shows the rotor cross section comparison between the proposed virtual SPM model and the original IPM. Their FEA results are compared in Figure 5b,c, showing the same radial air gap flux distribution. The V-type IPM had the same rotor OD, pole-arc coefficient α_p, magnet thickness h_m, and relative permeability μ_r as the virtual SPM. The magnet remanence B_{er} of the virtual SPM was adjusted to obtain equivalent flux density distribution in the stators as in Figure 5b, and the similar slotless radial air-gap flux density curve as illustrated in Figure 5c.

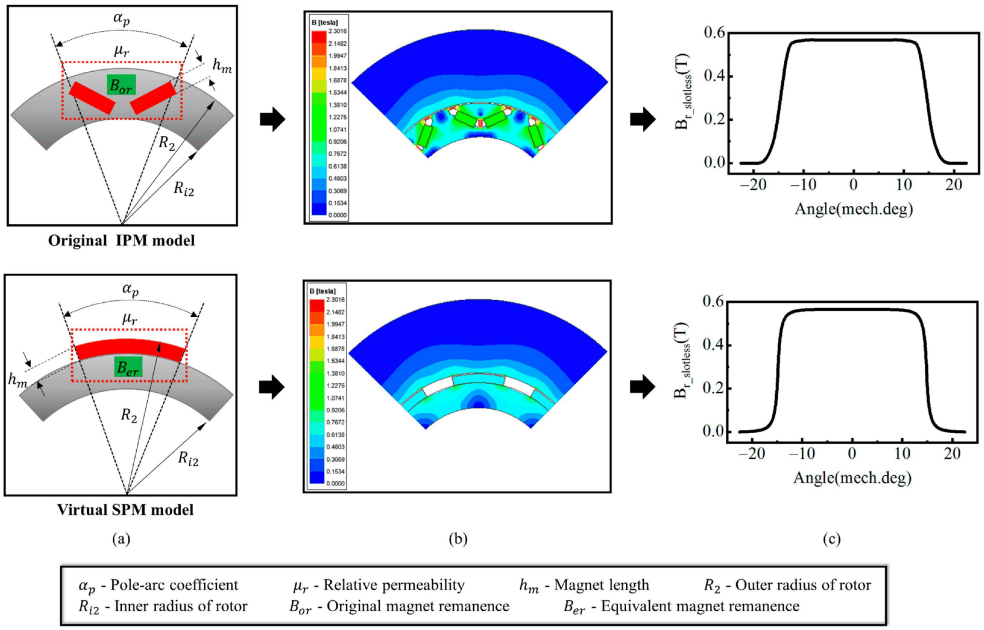

Figure 5. Comparison between original IPM and its equivalent virtual SPM: (**a**) Rotor cross section comparison. (**b**) Equivalent flux density distribution. (**c**) Slotless radial air-gap flux density curve.

With the proposed virtual SPM model, the Laplace's equation and quasi-Poisson equation could then be used to predict 2D slotless radial air-gap flux density of IPM machine. So that the resulting flux density analytical expression could accurately produce the trapezoidal shaped distribution, as shown in the FEA results in Figure 5c. The radial flux density in the middle of air gap ($r = R_{i1} - \delta/2$) was then derived as:

$$\begin{aligned} B_{r\_2D}(r,\theta) = & \sum_{n=1,3,5\ldots}^{\infty} \frac{\mu_0 M_n}{\mu_r} \cdot \frac{np}{(np)^2-1} \\ & \cdot \left\{ \frac{(np-1)+2\left(\frac{R_2}{R_m}\right)^{np+1}-(np+1)\left(\frac{R_2}{R_m}\right)^{2np}}{\frac{\mu_r+1}{\mu_r}\cdot\left[1-\left(\frac{R_2}{R_{i1}}\right)^{2np}\right]-\frac{\mu_r-1}{\mu_r}\cdot\left[\left(\frac{R_m}{R_{i1}}\right)^{2np}-\left(\frac{R_2}{R_m}\right)^{2np}\right]} \right\} \\ & \cdot \left[\left(\frac{R_m}{R_{i1}}\right)^{np+1}\cdot\left(\frac{r}{R_{i1}}\right)^{np-1}+\left(\frac{R_m}{r}\right)^{np+1}\right]\cdot\cos(np\theta) \end{aligned} \tag{5}$$

where

$$M_n = 2\left(\frac{B_{er}}{\mu_0}\right)\alpha_p \frac{\sin\left(\frac{n\pi\alpha_p}{2}\right)}{\frac{n\pi\alpha_p}{2}} \tag{6}$$

$$R_2 = R_m - h_m \tag{7}$$

$$R_m = R_{i1} - \delta \tag{8}$$

$$R_{i1} = D_{i1}/2 \tag{9}$$

where R_2 is the outer radius of rotor, R_{i1} is the inner radius of stator, and R_m is the radius of the magnets.

As introduced earlier, B_{er} in the virtual SPM was to be determined for (5), so that it obtained the equivalent flux distribution as the original IPM. Figure 6 introduces the process of obtaining B_{er}. It is to be noted that even though the 1D LMC method used for IPM analytical solution only produced the inaccurate rectangle shaped flux density distribution, its flat top value was correct. Therefore, the value of B_{er} in the virtual SPM was iteratively adjusted, until its trapezoid flat top values by (5) was equal to the rectangle flat top values obtained by the 1D LMC model (2) of the original IPM. In Figure 6, the flat top values by (2) and (5) are defined as $B_{r\_amp\_1D}$ and $B_{r\_amp\_2D}$, respectively.

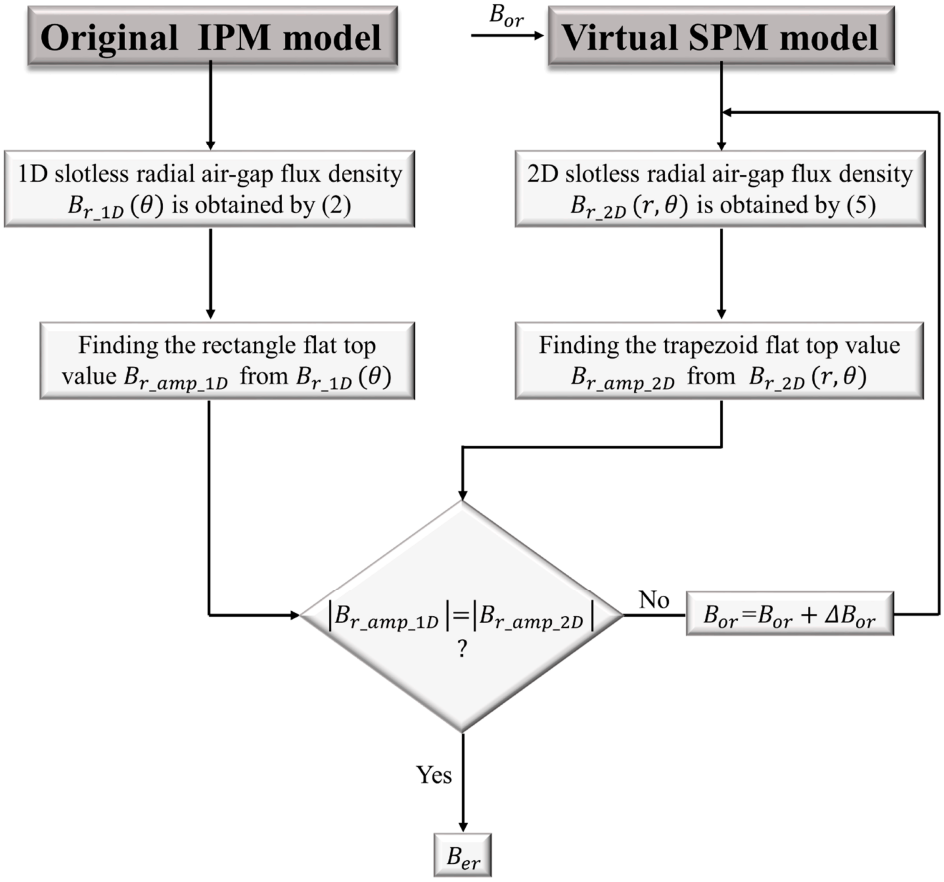

Figure 6. The iterative process of obtaining the equivalent magnet remanence B_{er}.

3.2. Relative Permeance Function Based on the 2D Model

Herein, the same virtual SPM as in Figure 5a was used to represent the original IPM model, while its PM thickness was set to zero ($h_m = 0$), as in Figure 7. Then, the 2D permeance model could be derived for IPM. The single tooth pitch model for permeance expression derivation is shown in Figure 8. The air gap flux density distribution near the slot opening was approximated by a cosine function.

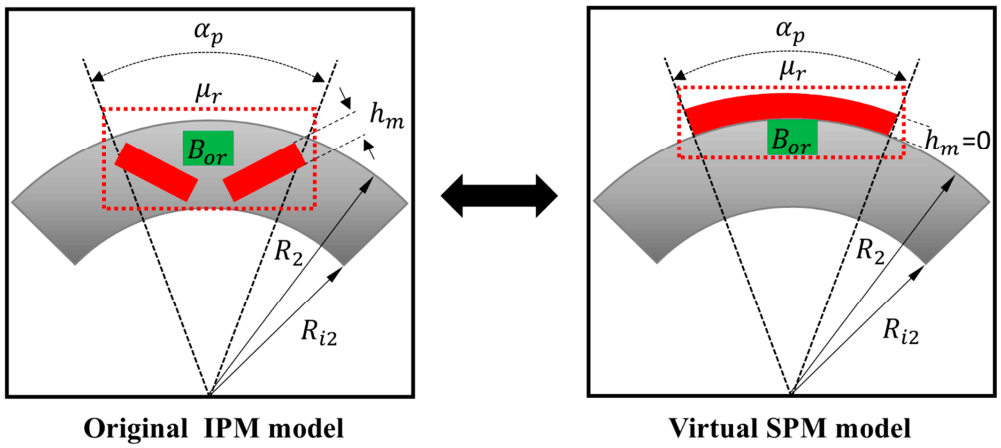

Figure 7. The equivalent virtual SPM model for IPM relative permeance 2D model derivation.

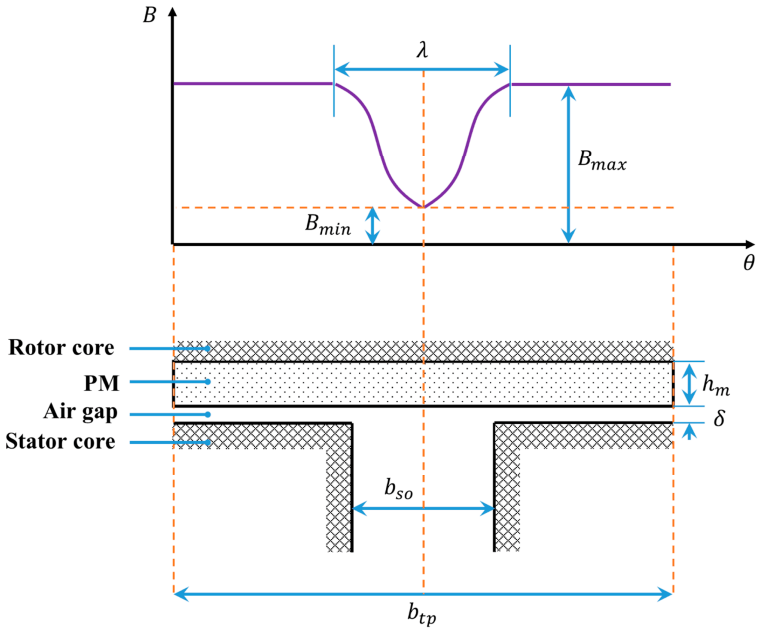

Figure 8. The single tooth pitch model for permeance expression derivation.

As discussed previously, the assumption of constant MMF sources brings significant errors in the IPM 1D model. Therefore, the 2D model derivation used the carter coefficient to tackle the interpolar leakage flux, and the Schwarz-Christoffel Transformation to address the complication that the interface between the PMs and the air gap was no longer an equipotential surface.

By ignoring the interaction between the adjacent slots, the corresponding 2D relative permeance function $\widetilde{G}_{2D}(r,\theta)$ based on the virtual SPM model could be derived by the following Fourier series as:

$$\widetilde{G}_{2D}(r,\theta) = \mathrm{A}_0 + \sum_{n=1}^{\infty} \mathrm{A}_n \cos(nN_s(\theta + \theta_{sa})) \tag{10}$$

where θ_{sa} is the relative angle between stator slot center and the axis of phase A. A_0 and A_n can be deduced as:

$$\mathrm{A}_0 = 1 - \frac{\lambda}{b_{tp}}\kappa(r) \tag{11}$$

$$\mathrm{A}_n = -\frac{2}{\pi n} \cdot \kappa(r) \cdot \sin\left(\pi n \frac{\lambda}{b_{tp}}\right) \cdot \left[1 + \frac{n^2}{\left(\frac{b_{tp}}{\lambda}\right)^2 - n^2}\right] \tag{12}$$

where $\kappa(r)$ is a defined function derived by Schwarz-Christoffel Transformation, λ is the Carter coefficient, and b_{tp} is the stator tooth pitch. $\kappa(r)$ and λ are further expressed as:

$$\kappa(r) = \frac{1}{2}\left[1 - \frac{1}{\sqrt{1 + \left(\frac{b_{so}}{2\delta'}\right)^2 (1 + v^2)}}\right] \tag{13}$$

$$\lambda = \frac{\eta \cdot \delta'}{\kappa(r)} \tag{14}$$

where

$$\delta' = \delta + \frac{h_m}{\mu_r} = \delta \tag{15}$$

$$\eta = \frac{4}{\pi}\left[\left(\frac{b_{so}}{2\delta}\right)\cdot \arctan\left(\frac{b_{so}}{2\delta}\right) - \mathrm{In}\sqrt{1+\left(\frac{b_{so}}{2\delta}\right)^2}\right] \tag{16}$$

where b_{so} is the slot-opening width, $h_m = 0$ in the virtual SPM model.

Note that v is an intermediate variable further determined by:

$$y\frac{\pi}{b_{so}} = \frac{1}{2}In\left[\frac{\sqrt{a^2+v^2}+v}{\sqrt{a^2+v^2}-v}\right] + \frac{2\delta}{b_{so}}\arctan\left(\frac{2\delta}{b_{so}}\frac{v}{\sqrt{a^2+v^2}}\right) \tag{17}$$

where

$$a^2 = 1+\left(\frac{2\delta}{b_{so}}\right)^2$$
$$y = r - R_{i1} + \delta \text{ for an internal rotor}$$

Additionally, note that v was the only unknown in (17), and after v was solved, the Expression (13) was completed.

By deriving the IPM's virtual SPM equivalence, the IPM relative permeance 2D model was introduced.

Figure 9 shows that the analytical results from the IPM relative permeance 2D model derived with the proposed virtual SPM were in good agreement with FEA results, while the trapezoid flat top values and the trough values of 1D model were much smaller than that of FEA. It is also instructive to see the minimum value of relative permeance dependence on the radius r from Figure 10, where the permeance value (the lowest) in the center of the slot opening were compared among slotless, 1D, and improved 2D models. The slotless model returned the constant value 1, and the 1D model returned a constant much lower than the correct value. Only the proposed 2D model shows the correct trend that the relative permeance was dependent on radius r.

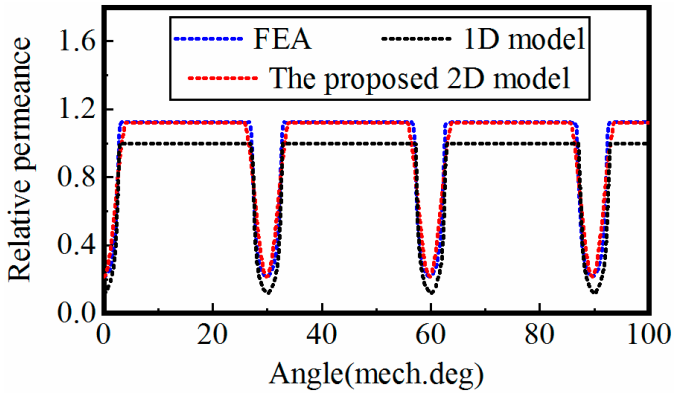

Figure 9. Permeance analytical results comparison with FEA results ($r = R_{i1} - \delta/2$).

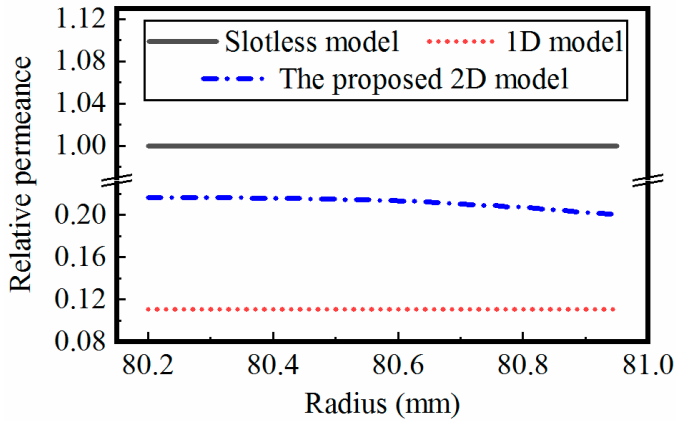

Figure 10. The minimum value of relative permeance and its dependence on the radius.

3.3. Slotted Radial Air-Gap Flux Density

Then, the actual slotted radial air gap flux density $B_{r\_2D\_slotted}(r,\theta)$ considering the slot-opening effect was obtained by the product of 2D slotless radial air-gap flux density and 2D relative permeance function as:

$$B_{r\_2D\_slotted}(r,\theta) = B_{r\_2D}(r,\theta) \cdot \widetilde{G}_{2D}(r,\theta) \tag{18}$$

Figure 11 shows the comparison of the slotted radial air gap flux density distributions using different methods. Obviously, the proposed 2D analytical model returned almost identical results to FEA, while the 1D analytical model had obvious errors that had significant impacts on the subsequent cogging torque analytical results.

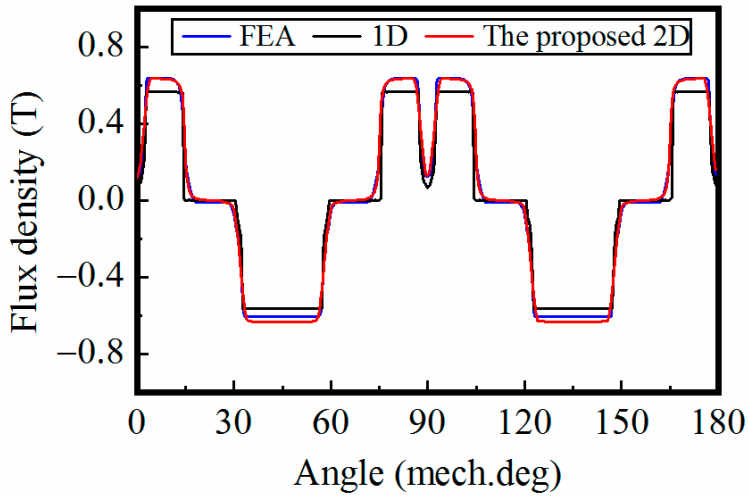

Figure 11. The slotted radial flux density distributions in the middle of air gap.

3.4. Analytical Model of the IPM Cogging Torque

Based on the proposed 2D models for both slotless radial air gap flux density and relative permeance, the accurate cogging torque expression could then be obtained by the net lateral force method and superposition.

The net cogging torque at any rotor position produced by the single slot can be calculated as:

$$T_{sc}(\alpha) = \frac{L_{ef}}{2\mu_0}\left[\begin{array}{l} \int_{\frac{-\theta_{so}}{2}}^{0} [B_{r\_2D\_slotted}(r,\theta)]^2 \cdot [R_{i1} + r_s(\theta)] \cdot R_{i1} d\theta \\ -\int_{0}^{\frac{\theta_{so}}{2}} [B_{r\_2D\_slotted}(r,\theta)]^2 \cdot [R_{i1} + r_s(\theta)] \cdot R_{i1} d\theta \end{array}\right]_{r=R_{i1}-\delta/2} \tag{19}$$

where α is the relative position angle between the rotor and the stator slot, θ is the circumferential direction angle, μ_0 is the vacuum permeability, and L_{ef} is the machine's active length.

The corresponding assumptions will be given as follows: the flux lines pass radially in the air gap regions and get into the stator teeth vertically in the circular paths in the slot opening regions. Due to the limited height of stator tooth tips, many flux lines near the center of slot-openings cannot enter the stator tooth tips when the slot-opening width is larger. Therefore, the function of $r_s(\theta)$ can be given by the following expression:

$$r_s(\theta) = \begin{cases} 0 & -\left(\frac{\frac{b_{so}}{2}-h_{stt}}{R_{i1}}\right) \le \theta \le \frac{\frac{b_{so}}{2}-h_{stt}}{R_{i1}} \\ \frac{b_{so}}{2} - R_{i1}|\theta| & \frac{\frac{b_{so}}{2}-h_{stt}}{R_{i1}} \le \theta \le \frac{b_{so}}{2R_{i1}} \ \ or \ \ -\frac{b_{so}}{2R_{i1}} \le \theta \le -\left(\frac{\frac{b_{so}}{2}-h_{stt}}{R_{i1}}\right) \\ 1 & \frac{b_{so}}{2R_{i1}} \le \theta \le \frac{b_{tp}}{R_{i1}} \ \ or \ \ -\frac{b_{tp}}{R_{i1}} \le \theta \le -\frac{b_{so}}{2R_{i1}} \end{cases} \tag{20}$$

where b_{so} is the slot-opening width, h_{stt} is the height of stator tooth tip, and b_{tp} is the stator tooth pitch.

Equation (19) can be applied to each slot. The total cogging torque for a machine can be obtained by superposition as:

$$T_{cog}(\alpha) = \sum_{n=1}^{\infty} T_{scn} \frac{\sin 2p\pi n}{\sin \frac{2p\pi}{N_s} n} \sin\left(2pn\alpha - \pi \frac{2p}{N_s} n\right) \tag{21}$$

where T_{scn} is the Fourier coefficient obtained from (19).

When $2p/N_s$ is the integral number, the total cogging torque is:

$$T_{cog}(\alpha) = N_s \sum_{n=1}^{\infty} T_{scn} \sin 2pn\alpha = N_s \sum_{n=1}^{\infty} T_{scn} \sin N_c n\alpha \tag{22}$$

where N_c is the least common multiple between the stator slots N_s and the rotor poles $2p$.

When $2p/N_s$ is the fractional number, the total cogging torque is:

$$T_{cog}(\alpha) = \sum_{i=1}^{\infty} N_s T_{scn} \Big|_{n=\frac{N_s}{\gamma} i} \sin N_c i\alpha \tag{23}$$

where γ is an integer and $\gamma = 2pN_s/N_c$.

3.5. Summary of the Proposed Analytical Model of IPM Cogging Torque

Figure 12 summarizes the complete derivation process of the proposed analytical model of IPM cogging torque. Herein, 2D analytical models for IPM slotless radial air gap flux density and relative permeance are proposed.

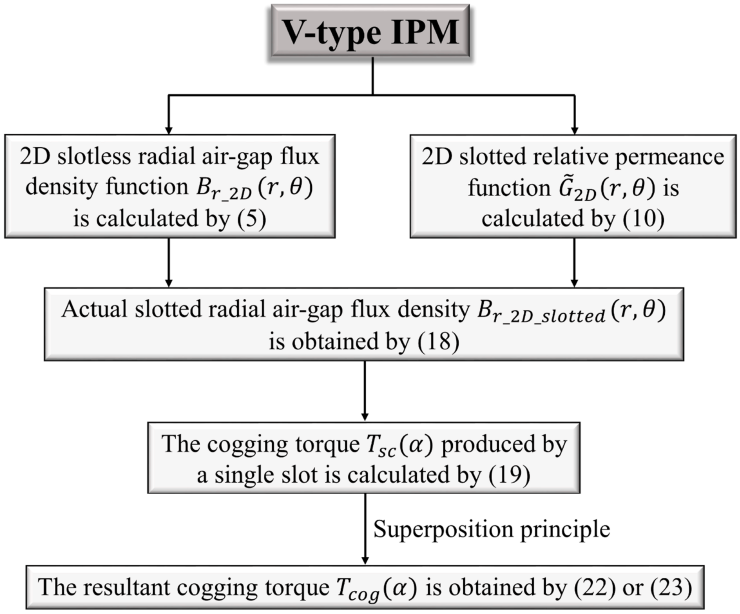

Figure 12. The complete derivation process of the proposed analytical model of IPM cogging torque.

4. Validation of the Proposed 2D Models for IPM

Herein, the cogging torque patterns predicted by the proposed IPM 2D models were compared with FEA results. Three machines with different pole-slot combinations were studied here, i.e., 8-pole, 12-slot (8P12S), 8-pole, 36-slot (8P36S), and 8-pole, 48-slot (8P48S). Additionally, the cogging torque optimization process using the proposed 2D analytical models was performed by adjusting the pole-arc coefficient and slot-opening coefficient, respectively.

4.1. Cogging Torque Patterns Predictions Compared with FEA

According to (23), the resultant cogging torque patterns of the V-type IPM machine were predicted and compared with FEA results, as shown in Figure 13. The analytical results of the proposed 2D model matched the FEA results well, while existing 1D models showed significant deviations.

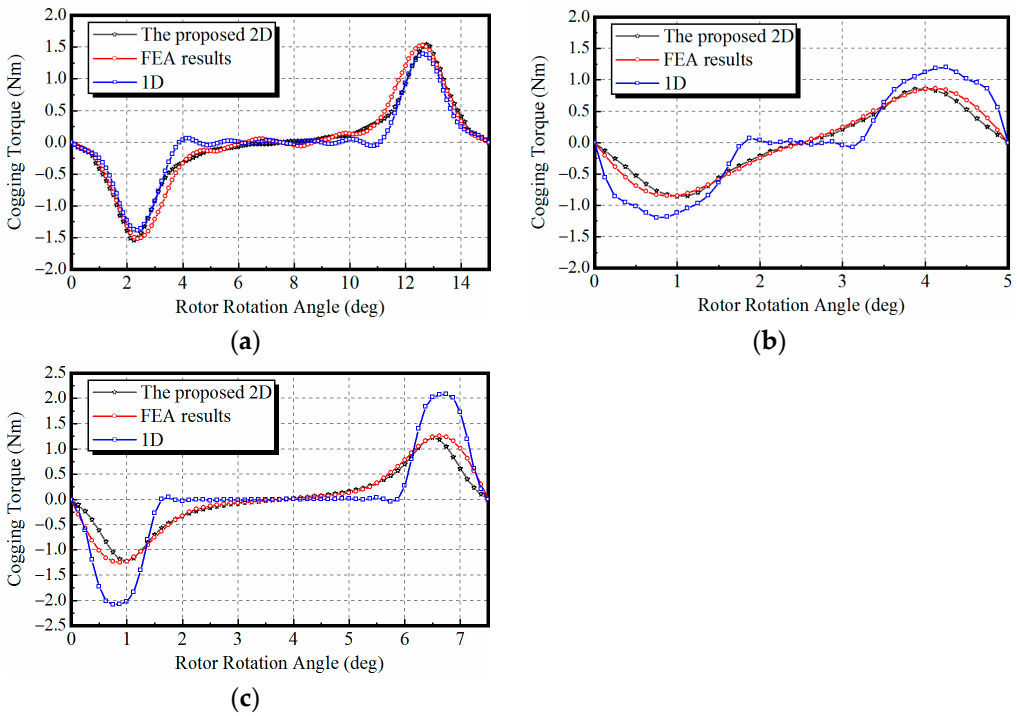

Figure 13. Comparison of FEA and analytical cogging torque waveforms, when pole-arc coefficient $\alpha_p = 0.63$, and slot-opening coefficient $\alpha_s = 0.18$: (**a**) 8P12S. (**b**) 8P36S. (**c**) 8P48S.

To further demonstrate that the proposed 2D analytical model is a highly efficient tool set in the design process of cogging torque optimization, the adjustment of pole-arc coefficient and slot-opening coefficient was performed and their impacts on the cogging torque were quantitatively studied subsequently.

4.2. IPM Cogging Torque Optimization Process Using the Proposed 2D Models (Pole-Arc Coefficient)

Figure 14 shows the trends of the cogging torque peak values when the pole-arc coefficient was adjusted by the angle and length of V-type PM. It can be seen that the analytical results from the proposed 2D model were in good agreement with FEA results. The optimal theoretical values of pole-arc coefficient for cogging torque reduction could be quickly found with the proposed 2D analytical models. By comparison, the previous IPM 1D analytical models could not accurately show the cogging torque trends during the pole-arc coefficient adjustment, so it failed to facilitate the design process of cogging torque optimization.

4.3. IPM Cogging Torque Optimization Process Using the Proposed 2D Models (Slot-Opening Coefficient)

Figure 15 shows the trends of the cogging torque peak values when the slot-opening was adjusted. It can be seen that the analytical results from the proposed 2D model were in good agreement with FEA results. The optimal theoretical values of slot-opening for cogging torque reduction could be quickly found with the proposed 2D analytical models. By comparison, the previous IPM 1D analytical models could not accurately show the cogging torque trends during the slot-opening adjustment, so it failed to facilitate the design process of cogging torque optimization.

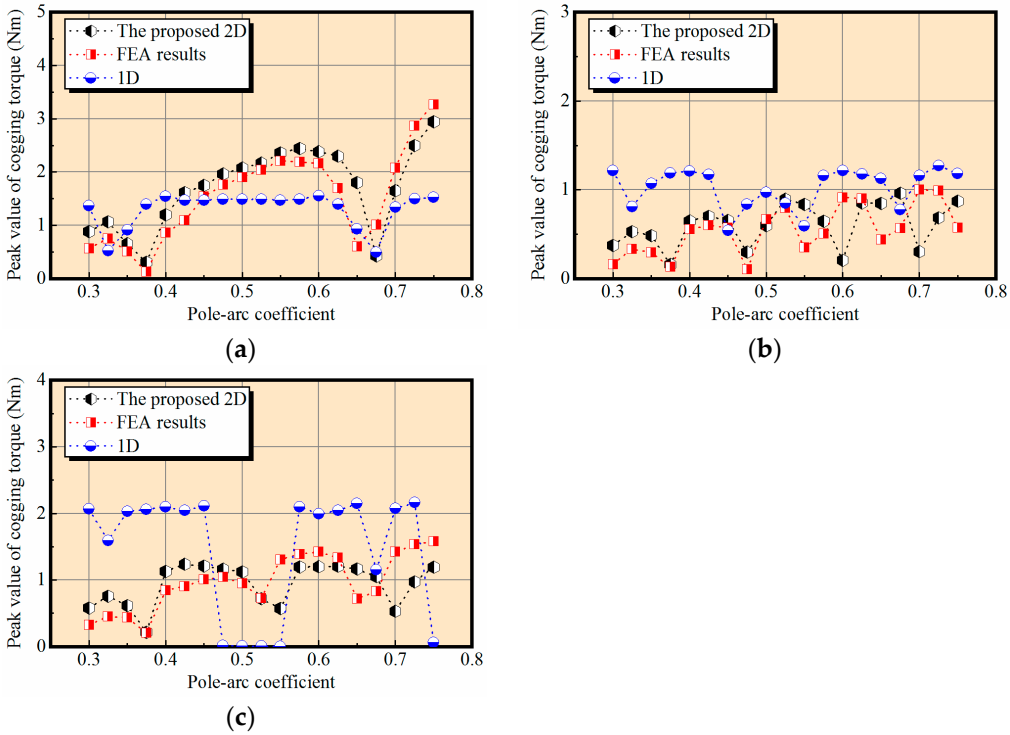

Figure 14. Cogging torque peak value trends with varying pole-arc coefficient, when slot-opening coefficient $\alpha_s = 0.18$: (**a**) 8P12S. (**b**) 8P36S. (**c**) 8P48S.

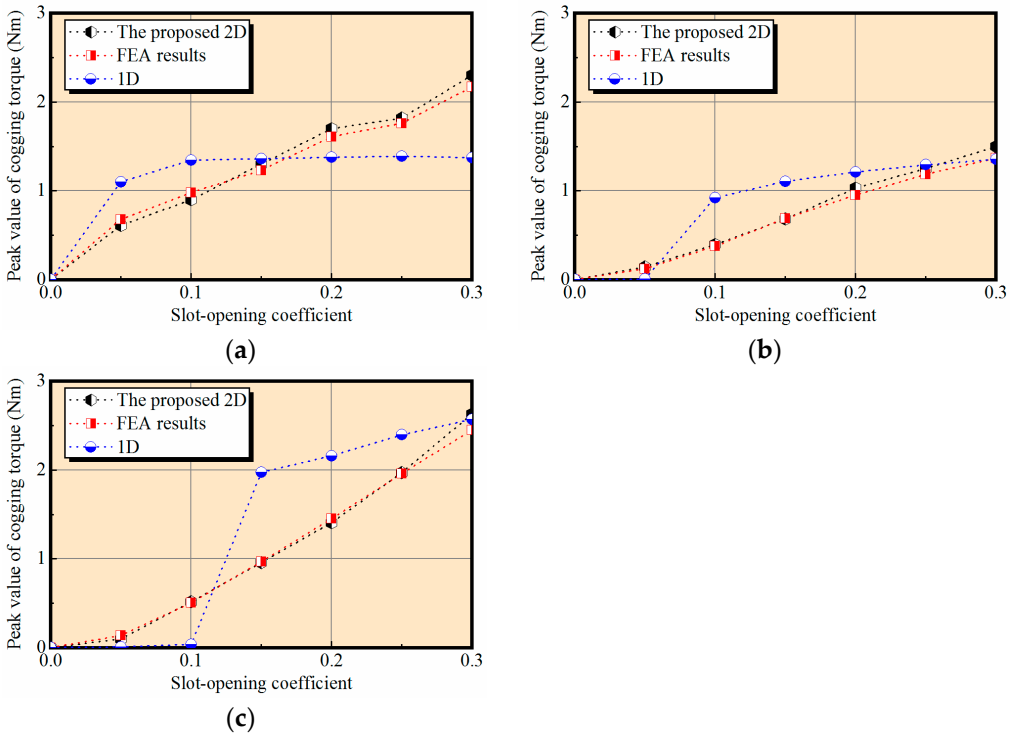

Figure 15. The cogging torque peak value trends with the varying slot-opening coefficient, when pole-arc coefficient $\alpha_p = 0.63$: (**a**) 8P12S. (**b**) 8P36S. (**c**) 8P48S.

As demonstrated above, the proposed 2D analytical model is a highly efficient tool set in the design process of cogging torque optimization. It is particularly useful when the cogging torque is to be optimized with tradeoffs between many combined factors. Meanwhile, it also shows similar accuracy to FEA tools.

5. Conclusions

In this paper, 2D analytical models have been proposed to accurately predict cogging torque in IPMs. The key was to first configure a virtual equivalence model with the same air gap flux distribution as the IPM, so that the accurate closed-form expressions of 2D models for both IPM slotless radial air gap flux density and relative permeance could be derived, despite all the complications from IPM severe magnetic saturation and leakage flux. With the virtual equivalence model, the Laplace's and quasi-Poisson equation could be applied directly to IPM to get 2D radial air gap flux density. The same virtual equivalence model was also applied to obtain 2D relative permeance. Finally, the cogging torque patterns predicted by the proposed IPM 2D models were validated by FEA results; meanwhile, the proposed method was further validated by FEA in multiple cogging torque optimization iterations of adjusting the pole-arc coefficient and slot-opening coefficient. In the validation process, the proposed method showed much better accuracy than the existing 1D based methods. As demonstrated, the proposed 2D analytical model is a highly efficient tool set in the design process of cogging torque optimization. It is particularly useful when the cogging torque is to be optimized with tradeoffs between many combined factors. Meanwhile, it also shows similar accuracy to FEA tools. In the proposed method, the 2D relative permeance function derivation is based on the assumption that the stator slot-opening is infinitely deep. This simplification would introduce slight deviation from the FEA results. To model the actual slot-opening depth, the relative permeance model, as used in this paper, is to be replaced by the accurate subdomain model. As 2D subdomain model has also not been applied to the IPM yet, it is possible that the virtual SPM methodology can be extended to fill this gap in the future work.

Author Contributions: Conceptualization, L.W.; methodology, L.W. and S.L.; software, L.W.; validation, L.W., S.L. and Y.C.; formal analysis, L.W.; investigation, L.W.; resources, S.L.; writing—original draft preparation, L.W.; writing—review and editing, L.W., S.L. and Y.C.; visualization, L.W.; supervision, S.L.; project administration, S.L.; funding acquisition, S.L. All authors have read and agreed to the published version of the manuscript.

Funding: This research was funded by the Fundamental Research Funds for the Central Universities, China under Grant 2022CDJXY-007.

Data Availability Statement: Not applicable.

Conflicts of Interest: The authors declare no conflict of interest.

References

1. Dosiek, L.; Pillay, P. Cogging torque reduction in permanent magnet machines. *IEEE Trans. Ind. Appl.* **2007**, *43*, 1565–1571. [CrossRef]
2. Breton, C.; Bartolome, J.; Benito, J.A.; Tassinario, G.; Flotats, I.; Lu, C.W.; Chalmers, B.J. Influence of machine symmetry on reduction of cogging torque in permanent-magnet brushless motors. *IEEE Trans. Magn.* **2000**, *36*, 3819–3823. [CrossRef]
3. Wu, L.J.; Zhu, Z.Q.; Staton, D.A.; Popescu, M.; Hawkins, D. Comparison of analytical models of cogging torque in surface-mounted PM machines. *IEEE Trans. Ind. Electron.* **2012**, *59*, 2414–2425. [CrossRef]
4. Wang, D.H.; Wang, X.H.; Qiao, D.W.; Pei, Y.; Jung, S.Y. Reducing Cogging Torque in Surface-Mounted Permanent-Magnet Motors by Nonuniformly Distributed Teeth Method. *IEEE Trans. Magn.* **2011**, *47*, 2231–2239. [CrossRef]
5. Hwang, C.C.; John, S.B.; Wu, S.S. Reduction of cogging torque in spindle motors for CD-ROM drive. *IEEE Trans. Magn.* **1998**, *34*, 468–470. [CrossRef]
6. Zhu, Z.Q.; Ruangsinchaiwanich, S.; Chen, Y.; Howe, D. Evaluation of superposition technique for calculating cogging torque in permanent-magnet brushless machines. *IEEE Trans. Magn.* **2006**, *42*, 1597–1603. [CrossRef]
7. Zhu, Z.Q.; Ruangsinchaiwanich, S.; Schofield, N.; Howe, D. Reduction of cogging torque in interior-magnet brushless machines. *IEEE Trans. Magn.* **2003**, *39*, 3238–3240. [CrossRef]
8. Bianchini, C.; Immovilli, F.; Lorenzani, E.; Bellini, A.; Davoli, M. Review of design solutions for internal permanent-magnet machines cogging torque reduction. *IEEE Trans. Magn.* **2012**, *48*, 2685–2693. [CrossRef]
9. Choi, J.S.; Izui, K.; Nishiwaki, S.; Kawamoto, A.; Nomura, T. Topology optimization of the stator for minimizing cogging torque of IPM motors. *IEEE Trans. Magn.* **2011**, *47*, 3024–3027. [CrossRef]
10. Ko, H.S.; Kim, K.J. Characterization of noise and vibration sources in interior permanent-magnet brushless DC motors. *IEEE Trans. Magn.* **2004**, *40*, 3482–3489. [CrossRef]

11. Islam, R.; Husain, I.; Fardoun, A.; McLaughlin, K. Permanent-magnet synchronous motor magnet designs with skewing for torque ripple and cogging torque reduction. *IEEE Trans. Ind. Appl.* **2009**, *45*, 152–160. [CrossRef]
12. Ishikawa, T.; Slemon, G.R. A method of reducing ripple torque in permanent-magnet motors without skewing. *IEEE Trans. Magn.* **1993**, *29*, 2028–2031. [CrossRef]
13. Hwang, S.M.; Eom, J.B.; Hwang, G.B.; Jeong, W.B.; Jung, Y.H. Cogging torque and acoustic noise reduction in permanent magnet motors by teeth pairing. *IEEE Trans. Magn.* **2000**, *36*, 3144–3146. [CrossRef]
14. Jahns, T.M.; Soong, W.L. Pulsating torque minimization techniques for permanent magnet AC motor drives-A review. *IEEE Trans. Ind. Electron.* **1996**, *43*, 321–330. [CrossRef]
15. Bianchi, N.; Bolognani, S. Design techniques for reducing the cogging torque in surface-mounted PM motors. *IEEE Trans. Ind. Appl.* **2002**, *38*, 1259–1265. [CrossRef]
16. Lukaniszyn, M.; Jagiela, M.; Wrobel, R. Optimization of permanent magnet shape for minimum cogging torque using a genetic algorithm. *IEEE Trans. Magn.* **2004**, *40*, 1228–1231. [CrossRef]
17. Arand, S.J.; Ardebili, M. Cogging torque reduction in axial-flux permanent magnet wind generators with yokeless and segmented armature by radially segmented and peripherally shifted magnet pieces. *Renew. Energy* **2016**, *99*, 95–106. [CrossRef]
18. Abbaszadeh, K.; Alam, F.R.; Teshnehlab, M. Slot opening optimization of surface mounted permanent magnet motor for cogging torque reduction. *Energy Convers. Manag.* **2012**, *55*, 108–115. [CrossRef]
19. Liu, T.; Huang, S.D.; Gao, J.; Lu, K.Y. Cogging torque reduction by slot-opening shift for permanent magnet machines. *IEEE Trans. Magn.* **2013**, *49*, 4028–4031. [CrossRef]
20. Koh, C.S.; Seol, J.S. New cogging-torque reduction method for brushless permanent-magnet motors. *IEEE Trans. Magn.* **2003**, *39*, 3503–3506.
21. Kim, T.H.; Won, S.H.; Bong, K.; Lee, J. Reduction of cogging torque in flux-reversal machine by rotor teeth pairing. *IEEE Trans. Magn.* **2005**, *41*, 3964–3966.
22. Zhu, L.; Jiang, S.Z.; Zhu, Z.Q.; Chan, C.C. Analytical modeling of open-circuit air-gap field distributions in multisegment and multilayer interior permanent-magnet machines. *IEEE Trans. Magn.* **2009**, *45*, 3121–3130. [CrossRef]
23. Lovelace, E.C.; Jahns, T.M.; Lang, J.H. A saturating lumped-parameter model for an interior PM synchronous machine. *IEEE Trans. Ind. Appl.* **2002**, *38*, 645–650. [CrossRef]
24. Mi, C.T.; Filippa, M.; Liu, W.G.; Ma, R.Q. Analytical method for predicting the air-gap flux of interior-type permanent-magnet machines. *IEEE Trans. Magn.* **2004**, *40*, 50–58. [CrossRef]
25. Qu, R.H.; Lipo, T.A. Analysis and modeling of air-gap and zigzag leakage fluxes in a surface-mounted permanent-magnet machine. *IEEE Trans. Ind. Appl.* **2004**, *40*, 121–127. [CrossRef]
26. Zhu, Z.Q.; Howe, D.; Chan, C.C. Improved analytical model for predicting the magnetic field distribution in brushless permanent-magnet machines. *IEEE Trans. Magn.* **2002**, *38*, 229–238. [CrossRef]
27. Rahideh, A.; Korakianitis, T. Analytical calculation of open-circuit magnetic field distribution of slotless brushless PM machines. *Int. J. Electr. Power* **2013**, *44*, 99–114. [CrossRef]
28. Kim, U.; Lieu, D.K. Magnetic field calculation in permanent magnet motors with rotor eccentricity: With slotting effect considered. *IEEE Trans. Magn.* **1998**, *34*, 2253–2266. [CrossRef]
29. Proca, A.B.; Keyhani, A.; El-Antably, A.; Lu, W.Z.; Dai, M. Analytical model for permanent magnet motors with surface mounted magnets. *IEEE Trans. Energy Convers.* **2003**, *18*, 386–391. [CrossRef]
30. Wang, X.; Li, Q.; Wang, S.; Li, Q. Analytical calculation of air-gap magnetic field distribution and instantaneous characteristics of brushless DC motors. *IEEE Trans. Energy Convers.* **2003**, *18*, 424–432. [CrossRef]
31. Zhu, Z.Q.; Howe, D. Instantaneous magnetic-field distribution in brushless permanent-magnet dc motors, part III: Effect of Stator Slotting. *IEEE Trans. Magn.* **1993**, *29*, 143–151. [CrossRef]
32. Seo, J.H.; Choi, H.S. Cogging torque calculation for IPM having single layer based on magnetic circuit model. *IEEE Trans. Magn.* **2014**, *50*, 1–4. [CrossRef]
33. Tsai, W.B.; Chang, T.Y. Analysis of flux leakage in a brushless permanent-magnet motor with embedded magnets. *IEEE Trans. Magn.* **1999**, *35*, 543–547. [CrossRef]
34. Hwang, C.C.; Cho, Y.H. Effects of leakage flux on magnetic fields of interior permanent magnet synchronous motors. *IEEE Trans. Magn.* **2001**, *37*, 3021–3024. [CrossRef]
35. Drabek, T.; Matras, A.; Skwarczynski, J. An analytical model of an electrical machine with internal permanent magnets. In *Lecture Notes in Electrical Engineering*; Gołębiowski, L., Mazur, D., Eds.; Springer: Berlin, Germany, 2015; Volume 324, pp. 215–239.
36. Drabek, T.; Skwarczynski, J. An analytical model of an electrical machine with internal permanent magnets. Part. II, The work of electric generator under an unbalanced load: Simulations and measurement verification. In *Lecture Notes in Electrical Engineering*; Mazur, D., Gołębiowski, M., Korkosz, M., Eds.; Springer: Berlin, Germany, 2018; Volume 452, pp. 87–109.